J. Fluid Mech. (2023), *vol*. 970, A26, doi:10.1017/jfm.2023.620

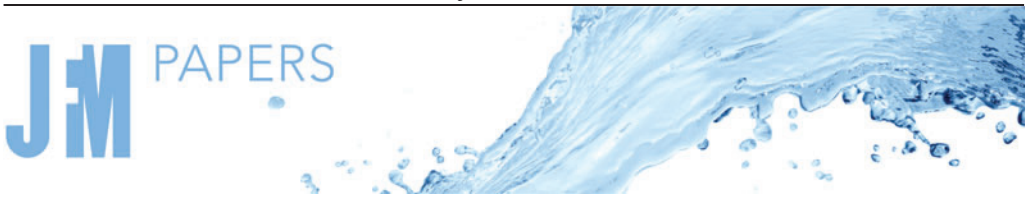

Role of internal structures within a vortex in helicity dynamics

Weiyu Shen[1], Jie Yao[2], Fazle Hussain[2] and Yue Yang[1,3,†]

[1]State Key Laboratory for Turbulence and Complex Systems, College of Engineering, Peking University, Beijing 100871, PR China

[2]Department of Mechanical Engineering, Texas Tech University, Lubbock, TX 79409, USA

[3]HEDPS-CAPT and BIC-ESAT, Peking University, Beijing 100871, PR China

(Received 24 November 2022; revised 18 July 2023; accepted 24 July 2023)

Helicity, an invariant under ideal-fluid (Euler) evolution, has a topological interpretation in terms of writhe and twist for a closed vortex tube, but accurately quantifying twist is challenging in viscous flows. With a novel helicity decomposition, we present a framework to construct the differential twist that establishes the theoretical relation between the total twisting number and the local twist rate of each vortex surface. This framework can characterize coiling vortex lines and internal structures within a vortex – important in laminar–turbulence transition, and in vortex instability, reconnection and breakdown. As a typical example, we explore the dynamics of vortex rings with differential twist via direct numerical simulation (DNS) of the Navier–Stokes equations. Two twist waves with opposite chiralities propagate towards each other along the ring and then collide whence the local twist rate rapidly surges. Local vortex surfaces are squeezed into a disk-like dipole structure containing coiled vortex lines, leading to vortex bursting. We derive a Burgers-equation-like model to quantify this process, which predicts a bursting time that agrees well with DNS.

Key words: topological fluid dynamics, vortex dynamics

1. Introduction

A complex flow field can be modelled as a collection of flux tubes, such as hydrodynamic flows (Moffatt & Tsinober 1992; Kleckner & Irvine 2013), superfluids (Koplik & Levine 1996; Kleckner, Kauffman & Irvine 2016) and plasmas (Cirtain *et al.* 2013). In particular, the vortex tube is a candidate elementary structure of turbulence (Hussain 1986; Moffatt, Kida & Ohkitani 1994; Pullin & Saffman 1998) (see figure 1*a*). Prototypical examples include rings in jets and wakes, and 'typical eddies' in turbulent boundary layers

† Email address for correspondence: yyg@pku.edu.cn

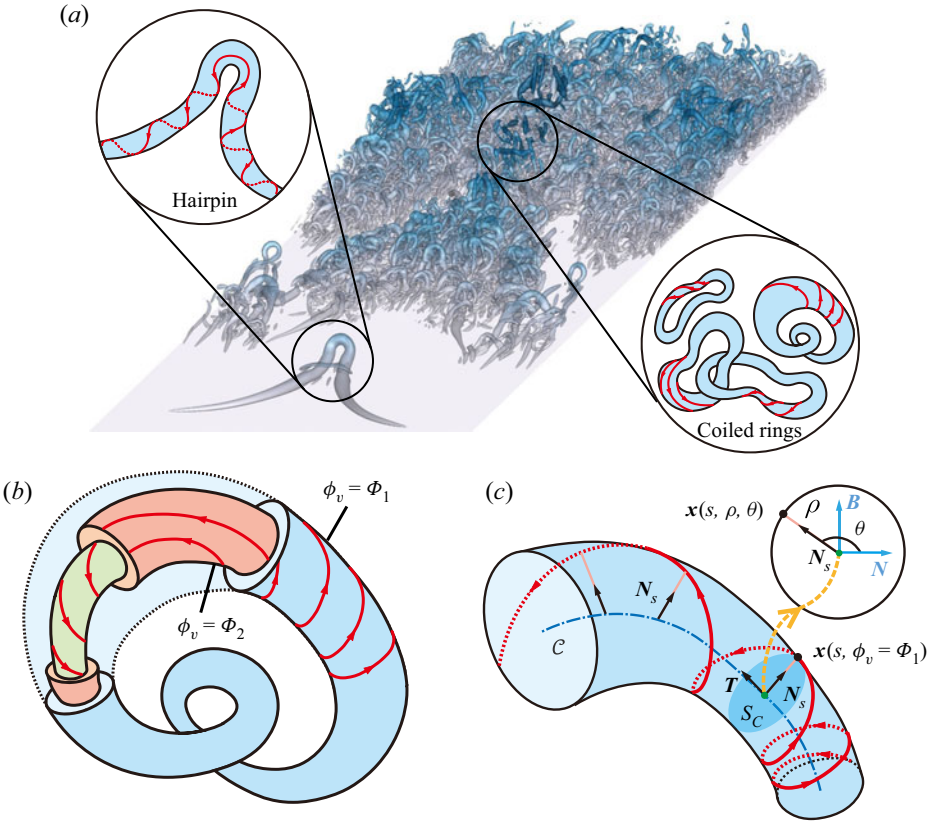

Figure 1. Schematic of closed vortex tubes with complex internal structures in transition and turbulence. (*a*) Conceptual model of the hairpin vortex in boundary layer transition and a collection of coiled and linked vortex rings in fully developed turbulence, where the flow visualization data were reported in Zheng, Yang & Chen (2016). (*b*) Closed vortex tube with differential twist on coaxial vortex surfaces and along the vortex centreline. The vortex surfaces are represented by VSF isosurfaces of different isocontour values, with embedded vortex lines (red solid). (*c*) A segment of the vortex tube in (*b*), where the vorticity is constructed based on the curved cylindrical coordinates (s, ρ, θ), and the vortex centreline $\mathcal{C}$ (blue dash-dotted) is described in the Frenet–Serret frame $(\boldsymbol{T}, \boldsymbol{N}, \boldsymbol{B})$.

(Robinson 1991). Vortex line coiling within a vortex tube – a topological manifestation of the helicity (Moffatt 1969; Moffatt & Ricca 1992) – plays an essential role in flow evolution, such as laminar–turbulence transition (Fritts, Arendt & Andreassen 1998; Ruan *et al.* 2022), vortex instability (Mayer & Powell 1992; Pradeep & Hussain 2001) and vortex reconnection (Zhao *et al.* 2021; Yao & Hussain 2022) and breakdown (Leibovich 1978).

Coiled vortex lines in a vortex tube can generate twist-wave packets, and their propagation and collision (Melander & Hussain 1994) can lead to bursting – causing an increase in the local enstrophy and energy dissipation. Vortex bursting has been found in aircraft trailing vortices (Tombach 1973), and addressed in theoretical (Arendt, Fritts & Andreassen 1997), experimental (Cuypers, Maurel & Petitjeans 2003) and numerical studies, but most are restricted to the configuration of vortex columns (Melander & Hussain 1994; Ji & van Rees 2022). By contrast, the vortex ring is more common in practical flows (Shariff & Leonard 1992) and has a well-defined topological interpretation of helicity in terms of the writhe W_r and twist T_w (Moffatt & Ricca 1992).

Helicity and its decomposition provide a powerful diagnostic tool to understand the complex three-dimensional (3-D) flow dynamics.

Whether helicity conservation can be extended to real dissipative flows is of particular interest and has been extensively studied recently (Kleckner & Irvine 2013; Scheeler *et al.* 2017; Kerr 2018*a*; Meng, Shen & Yang 2023). For example, Kleckner & Irvine (2013) experimentally observed that the knotted vortex is quite unstable and transferred to unlinked, coiled vortex rings through viscous reconnection. Numerical studies (Yao, Yang & Hussain 2021; Zhao *et al.* 2021) reveal that the helicity is not conserved during this process: while the initial writhe helicity is destroyed, the local twist rapidly surges at the reconnection site and then travels along the two separated rings. Therefore, studying twist-wave propagation and bursting can shed light not only on the extreme events in turbulence and transition (Moffatt 2021; Buaria & Pumir 2022), but also on the helicity dynamics of flux tubes with complex internal structures.

Studying twist-wave propagation and bursting in a vortex ring, or more generally, in a closed vortex tube, which can be knotted and linked (Ricca, Samuels & Barenghi 1999; Kleckner & Irvine 2013; Kerr 2018*b*; Yao *et al.* 2021), is challenging. First, it is difficult to directly construct a twist wave with a precise amplitude and distribution in a closed vortex tube. Second, in real flows, vortex lines within vortex tubes can have differential twist, i.e. different local twist rates on coaxial vortex surfaces or along the vortex centreline (see figure 1). The differential twist of vortex tubes with finite thickness cannot be characterized by the existing helicity decomposition (Moffatt & Ricca 1992), nor could it be directly measured in previous experiments (Kleckner & Irvine 2013; Scheeler *et al.* 2017; Angriman *et al.* 2021) or numerical simulations (Yao *et al.* 2021; Shen *et al.* 2022; Yao *et al.* 2022). The existing ribbon model (Moffatt & Tsinober 1992; Chui & Moffatt 1995) for twisting is restricted to a vortex tube with uniform twist, and it cannot characterize the internal twisting structure of vortex tubes.

We develop a novel helicity decomposition – along with numerical construction and measurement methods – for the differential twist. Moreover, the vortex-surface field (VSF) (Yang & Pullin 2010, 2011) is used to track and measure the twist of vortex lines. These methods facilitate the first quantitative study of bursting vortex rings with differential twist.

2. Twisting helicity for differential twist

We introduce here a definition for the differential twist and explain its relation to the helicity. The total helicity

$$H = \int_{\mathcal{V}} h \,\mathrm{d}\mathcal{V}, \tag{2.1}$$

is the volume integral of the helicity density $h = \boldsymbol{u} \cdot \boldsymbol{\omega}$ (Moreau 1961; Moffatt 1969), with the fluid velocity $\boldsymbol{u}$ and the vorticity $\boldsymbol{\omega} = \nabla \times \boldsymbol{u}$. The helicity of a closed vortex tube can be topologically morphed into $H = \Gamma^2(W_r + T_w)$ (Moffatt & Ricca 1992), with Γ the total circulation. Note that, while W_r can be obtained from a measurement of the vortex tube centrelines alone, it is difficult to characterize and directly measure T_w in practical flows. As sketched in figure 1(*b*), the nested coaxial vortex tubes without self-intersection are distinguished by different isosurfaces of a normalized VSF $\phi_v \in [0, 1]$. The limiting surface with $\phi_v = 1$ represents the vortex centreline $\mathcal{C}$. In figure 1(*c*), the vortex tube is represented in the curved cylindrical coordinate system (s, ρ, θ) (Xiong & Yang 2019, 2020). Here, $s \in [0, L_C)$ denotes the arclength along $\mathcal{C}$, L_C the length of $\mathcal{C}$, ρ the radial distance from $\mathcal{C}(s)$ and θ the azimuthal angle from $\boldsymbol{N}(s)$ in the plane S_C spanned by $\boldsymbol{N}(s)$ and $\boldsymbol{B}(s)$, where the unit normal $\boldsymbol{N}(s)$, binormal $\boldsymbol{B}(s)$ and tangent $\boldsymbol{T}(s)$ constitute the

Frenet–Serret frame on $\mathcal{C}$. For such vortex tubes with uniform $\boldsymbol{\omega}$ in θ, (s, ρ, θ) is simplified to (s, ϕ_v).

We derive the contribution of coiled vortex lines on different coaxial vortex surfaces to the total helicity. The twisting helicity (Moffatt & Ricca 1992) of an isolated closed vortex tube can be expressed as

$$H_T = \Gamma^2 T_w, \tag{2.2}$$

where Γ denotes the circulation and T_w the total twist number of the vortex tube. For closed vortex tubes with uniform twist along ϕ_v, the twisting number (Fuller 1971; Chui & Moffatt 1995)

$$T_w = \frac{1}{2\pi} \oint_{\mathcal{C}} (\boldsymbol{N}_s \times \boldsymbol{N}_s') \cdot \boldsymbol{T} \, \mathrm{d}s, \tag{2.3}$$

is defined by a ribbon model. Here, the ribbon edges are the vortex centreline $\mathcal{C}$ and a vortex line $\mathcal{C}^*$. Moreover, $\boldsymbol{N}_s$ denotes a radial unit vector from $\mathcal{C}$ pointing to $\mathcal{C}^*$ in plane S_C (see figure 1*c*), and $\boldsymbol{N}_s' = \mathrm{d}\boldsymbol{N}_s/\mathrm{d}s$; $\boldsymbol{T}$ is the unit tangent vector of $\mathcal{C}$. This definition requires that every vortex line has the same value of T_w calculated from (2.3), so it is restricted to characterizing a vortex tube with uniform twist or a differential twist along the vortex centreline.

In order to characterize the differential twist both along the vortex centreline and on different vortex surfaces, we establish a more complete definition of T_w than (2.3). For generalized closed tubes with differential twist, we introduce the local twist rate

$$\eta\,(s, \phi_v) = \left(\boldsymbol{N}_s \times \boldsymbol{N}_s'\right) \cdot \boldsymbol{T}, \tag{2.4}$$

for a vortex line on a vortex surface of ϕ_v at different locations, and the circulation

$$\Gamma_\phi = \Gamma_\phi(\phi_v) \in [0, \Gamma], \tag{2.5}$$

through the tube enclosed by a vortex surface of ϕ_v. If η is circumferentially uniform on each vortex surface, i.e. η is constant on the intersection of the isosurface of ϕ_v and the plane S_C normal to $\mathcal{C}$, we define the twisting number

$$T_\phi\,(\phi_v) = \frac{1}{2\pi} \oint_{\mathcal{C}} \eta\,(s, \phi_v)\ \mathrm{d}s, \tag{2.6}$$

for each vortex surface.

We first calculate the twisting helicity $\Delta H_T(\Phi)$ for a single vortex surface of $\phi_v = \Phi$ (see figure 2) with a given constant Φ. This surface with infinitesimal thickness has $\Gamma_\phi(\Phi)$ and $T_\phi(\Phi)$. As illustrated in figure 2

$$\Delta H_T(\Phi) = \bar{H}_{T,1} - \bar{H}_{T,2}, \tag{2.7}$$

of a twisted vortex tube can be obtained by the difference of twisting helicities for two adjacent co-axial virtual vortex tubes 1 and 2 with

$$\bar{\Gamma}_1 = \Gamma_\phi\,(\Phi)\,, \quad \bar{T}_{w,1} = T_\phi\,(\Phi)\,, \tag{2.8a,b}$$

and

$$\bar{\Gamma}_2 = \Gamma_\phi\,(\Phi + \Delta\phi_v)\,, \quad \bar{T}_{w,2} = T_\phi\,(\Phi)\,, \tag{2.9a,b}$$

respectively, where the overline denotes the quantity in a virtual tube. All co-axial vortex surfaces inside the two virtual tubes have the same twist distribution as the vortex surface

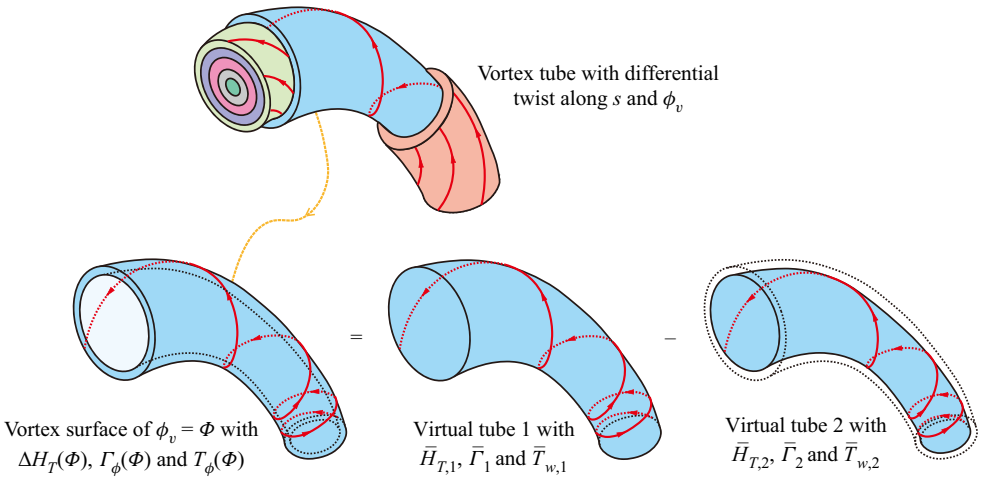

Figure 2. Schematic for calculating the twisting helicity of a vortex surface with infinitesimal thickness by two adjacent co-axial virtual tubes with uniform twist along ϕ_v. The vortex surface of $\phi_v = \Phi$ is peeled off from the vortex tube with differential twist along s and ϕ_v. All co-axial vortex surfaces inside the two virtual tubes have the same twist distribution as the vortex surface of $\phi_v = \Phi$.

$\phi_v = \Phi$, so the two virtual tubes have uniform twist along ϕ_v and their twisting helicities can be obtained by (2.2).

Substituting (2.2), (2.8*a*,*b*) and (2.9*a*,*b*) into (2.7) yields

$$\Delta H_T(\Phi) = \Gamma_\phi(\Phi)^2 T_\phi(\Phi) - \Gamma_\phi(\Phi + \Delta\phi_v)^2 T_\phi(\Phi). \tag{2.10}$$

Applying the Taylor expansion of $\Gamma_\phi(\Phi + \Delta\phi_v)$ to (2.10) yields

$$\Delta H_T(\Phi) = -2\Gamma_\phi(\Phi)\frac{\mathrm{d}\Gamma_\phi(\Phi)}{\mathrm{d}\phi_v} T_\phi(\Phi)\Delta\phi_v + O(\Delta\phi_v^2). \tag{2.11}$$

Then, we obtain

$$\frac{\mathrm{d}H_T(\Phi)}{\mathrm{d}\phi_v} = \lim_{\Delta\phi_v \to 0} \frac{\Delta H_T(\Phi)}{\Delta\phi_v} = -2\Gamma_\phi(\Phi)\frac{\mathrm{d}\Gamma_\phi(\Phi)}{\mathrm{d}\phi_v} T_\phi(\Phi). \tag{2.12}$$

Thus each vortex surface of ϕ_v in a vortex tube with differential twist along s and ϕ_v has

$$\mathrm{d}H_T(\phi_v) = -2\Gamma_\phi(\phi_v)\frac{\mathrm{d}\Gamma_\phi(\phi_v)}{\mathrm{d}\phi_v} T_\phi(\phi_v)\,\mathrm{d}\phi_v. \tag{2.13}$$

Finally, we obtain the total twisting helicity

$$H_T = -\frac{1}{\pi}\int_0^1 \Gamma_\phi(\phi_v)\frac{\mathrm{d}\Gamma_\phi(\phi_v)}{\mathrm{d}\phi_v}\left(\oint_{\mathcal{C}} \eta(s, \phi_v)\,\mathrm{d}s\right)\mathrm{d}\phi_v, \tag{2.14}$$

of a vortex tube with the total circulation Γ and differential twist along s and ϕ_v by the integration $\int \mathrm{d}H_T$ with (2.6), which is a circulation-weighted average of twisting numbers over all co-axial vortex surfaces. Substituting (2.14) into (2.2) yields

$$T_w = -\frac{1}{\pi\Gamma^2}\int_0^1 \Gamma_\phi(\phi_v)\frac{\mathrm{d}\Gamma_\phi(\phi_v)}{\mathrm{d}\phi_v}\left(\oint_{\mathcal{C}} \eta(s, \phi_v)\,\mathrm{d}s\right)\mathrm{d}\phi_v. \tag{2.15}$$

This equation is further verified with several numerical examples in Appendix A.

3. Construction of differential twist

We construct the vorticity field $\boldsymbol{\omega}$ for a closed vortex tube with differential twist. This construction method with its numerical algorithm is an extension of that in Xiong & Yang (2019, 2020) by incorporating variations of the core size and local twist rate in terms of s and ϕ_v.

First, the tube centreline $\mathcal{C}$ is described by a given parametric equation

$$\boldsymbol{x} = \boldsymbol{c}(s) + \rho\cos\theta\boldsymbol{N}(s) + \rho\sin\theta\boldsymbol{B}(s). \tag{3.1}$$

The Frenet–Serret formulas on $\mathcal{C}$ are

$$\left.\begin{aligned} \frac{\mathrm{d}\boldsymbol{T}}{\mathrm{d}s} &= \kappa\boldsymbol{N}, \\ \frac{\mathrm{d}\boldsymbol{N}}{\mathrm{d}s} &= -\kappa\boldsymbol{T} + \tau\boldsymbol{B}, \\ \frac{\mathrm{d}\boldsymbol{B}}{\mathrm{d}s} &= -\tau\boldsymbol{N}, \end{aligned}\right\} \tag{3.2}$$

where κ is the curvature and τ is the torsion of $\mathcal{C}$.

Based on coordinates (s, ρ, θ), we specify

$$\boldsymbol{\omega}(s,\rho,\theta) = \omega_s(s,\rho)\boldsymbol{e}_s + \omega_\rho(s,\rho,\theta)\boldsymbol{e}_\rho + \omega_\theta(s,\rho,\theta)\boldsymbol{e}_\theta, \tag{3.3}$$

of a vortex tube, where the local frame is spanned by unit vectors

$$\left.\begin{aligned} \boldsymbol{e}_s &= \boldsymbol{T}, \\ \boldsymbol{e}_\rho &= \cos\theta\boldsymbol{N} + \sin\theta\boldsymbol{B}, \\ \boldsymbol{e}_\theta &= -\sin\theta\boldsymbol{N} + \cos\theta\boldsymbol{B}. \end{aligned}\right\} \tag{3.4}$$

By setting the variable initial core size $\sigma(s)$ and local twist rate $\eta(s,\phi_v)$, vorticity components $\omega_s(s,\rho)$ and $\omega_\theta(s,\rho,\theta)$ are determined by introducing $\sigma(s)$ and $\eta(s,\phi_v)$ into the construction method in Xiong & Yang (2020) and Shen *et al.* (2022) and then $\omega_\rho(s,\rho,\theta)$ is solved from the divergence-free constraint. Thus the vorticity of closed vortex tubes with differential twist and variable thickness is specified as

$$\boldsymbol{\omega}(s,\rho,\theta) = \Gamma f(s,\rho)\left[\underbrace{\boldsymbol{e}_s}_{\textit{flux}} + \underbrace{\frac{\mathrm{d}\sigma(s)}{\mathrm{d}s}\frac{\rho\boldsymbol{e}_\rho}{\sigma(s)(1-\kappa(s)\rho\cos\theta)}}_{\textit{tube thickness}} + \underbrace{\frac{\rho\eta(s,\phi_v)\boldsymbol{e}_\theta}{1-\kappa(s)\rho\cos\theta}}_{\textit{twist}}\right], \tag{3.5}$$

with the Gaussian kernel function

$$f(s,\rho) = \begin{cases} \dfrac{1}{2\pi\sigma(s)^2}\exp\left[\dfrac{-\rho^2}{2\sigma(s)^2}\right], & s\in[0,L_C), \quad \rho\in[0,R_v), \\ 0, & s\in[0,L_C), \quad \rho\in[R_v,+\infty), \end{cases} \tag{3.6}$$

and the initial normalized VSF

$$\phi_v(s,\rho) = 2\pi\sigma(s)^2 f(s,\rho) \in [0,1], \tag{3.7}$$

where the three terms on the right-hand side of (3.5) represent the vorticity flux, tube thickness and twist terms of $\boldsymbol{\omega}$, respectively.

If $\kappa(s) = 0$ and $\eta(s, \phi_v) = 0$, (3.5) degenerates into the vorticity for a straight vortex tube with a variable core size (Ji & van Rees 2022). If $\sigma(s)$ and $\eta(s, \phi_v)$ are constants, (3.5) degenerates into a constant-thickness vortex tube with uniform twist (Xiong & Yang 2020; Shen *et al.* 2022).

As proved below, the vector field constructed by (3.5) is solenoidal, which can be used as a vorticity or magnetic field.

THEOREM 1. *The vector field $\boldsymbol{\omega}$ constructed by (3.5) is divergence free.*

Proof. In the curved cylindrical coordinate system, by applying the inverse function theorem to the Jacobian matrix (Xiong & Yang 2020) between (s, ρ, θ) and (x, y, z), we derive

$$\left.\begin{aligned} \nabla s &= \frac{\boldsymbol{T}}{1 - \kappa\rho\cos\theta}, \\ \nabla \rho &= \cos\theta \boldsymbol{N} + \sin\theta \boldsymbol{B}, \\ \nabla \theta &= \frac{-\tau}{1 - \kappa\rho\cos\theta}\boldsymbol{T} + \frac{1}{\rho}\left(-\sin\theta \boldsymbol{N} + \cos\theta \boldsymbol{B}\right). \end{aligned}\right\} \tag{3.8}$$

Taking the divergence of (3.3) yields

$$\nabla \cdot \boldsymbol{\omega} = \nabla \cdot (\omega_s \boldsymbol{e}_s) + \nabla \cdot (\omega_\rho \boldsymbol{e}_\rho) + \nabla \cdot (\omega_\theta \boldsymbol{e}_\theta), \tag{3.9}$$

and using (3.4) yields

$$\nabla \cdot (\omega_s \boldsymbol{e}_s) = \left(\frac{\partial \omega_s}{\partial s}\nabla s + \frac{\partial \omega_s}{\partial \rho}\nabla \rho\right)\boldsymbol{T} + \omega_s \frac{\mathrm{d}\boldsymbol{T}}{\mathrm{d}s} \cdot \nabla s, \tag{3.10}$$

$$\begin{aligned} \nabla \cdot (\omega_\rho \boldsymbol{e}_\rho) = &\left(\frac{\partial \omega_\rho}{\partial s}\nabla s + \frac{\partial \omega_\rho}{\partial \rho}\nabla \rho + \frac{\partial \omega_\rho}{\partial \theta}\nabla \theta\right)(\cos\theta \boldsymbol{N} + \sin\theta \boldsymbol{B}) \\ &+ \omega_\rho\left(-\sin\theta \nabla\theta \cdot \boldsymbol{N} + \cos\theta \frac{\mathrm{d}\boldsymbol{N}}{\mathrm{d}s} \cdot \nabla s + \cos\theta \nabla\theta \cdot \boldsymbol{B} + \sin\theta \frac{\mathrm{d}\boldsymbol{B}}{\mathrm{d}s} \cdot \nabla s\right), \end{aligned} \tag{3.11}$$

$$\begin{aligned} \nabla \cdot (\omega_\theta \boldsymbol{e}_\theta) = &\left(\frac{\partial \omega_\theta}{\partial s}\nabla s + \frac{\partial \omega_\theta}{\partial \rho}\nabla \rho + \frac{\partial \omega_\theta}{\partial \theta}\nabla \theta\right)(-\sin\theta \boldsymbol{N} + \cos\theta \boldsymbol{B}) \\ &+ \omega_\theta\left(-\cos\theta \nabla\theta \cdot \boldsymbol{N} - \sin\theta \frac{\mathrm{d}\boldsymbol{N}}{\mathrm{d}s} \cdot \nabla s - \sin\theta \nabla\theta \cdot \boldsymbol{B} + \cos\theta \frac{\mathrm{d}\boldsymbol{B}}{\mathrm{d}s} \cdot \nabla s\right). \end{aligned} \tag{3.12}$$

Substituting (3.2) and (3.4) into (3.10), (3.11) and (3.12), and considering the orthogonality of the Frenet–Serret frame yields

$$\left.\begin{aligned} \nabla \cdot (\omega_s \boldsymbol{e}_s) &= \frac{1}{1 - \kappa\rho\cos\theta}\frac{\partial \omega_s}{\partial s}, \\ \nabla \cdot (\omega_\rho \boldsymbol{e}_\rho) &= \frac{\partial \omega_\rho}{\partial \rho} + \frac{1 - 2\kappa\rho\cos\theta}{\rho(1 - \kappa\rho\cos\theta)}\omega_\rho, \\ \nabla \cdot (\omega_\theta \boldsymbol{e}_\theta) &= \frac{1}{\rho}\frac{\partial \omega_\theta}{\partial \theta} + \frac{\kappa\sin\theta}{1 - \kappa\rho\cos\theta}\omega_\theta. \end{aligned}\right\} \tag{3.13}$$

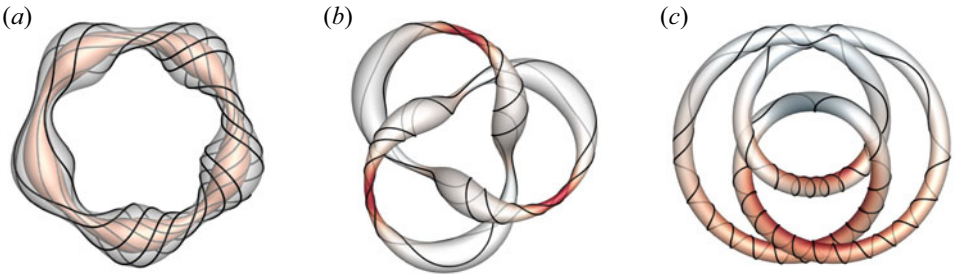

Figure 3. Closed vortex tubes with various internal structures. These closed vortex tubes with arbitrary topology, differential twist and variable thickness are constructed by (3.5): (*a*) trivial ring, (*b*) trefoil knot and (*c*) figure-eight knot. They are visualized by VSF isosurfaces with embedded vortex lines. The inner and outer tubes in (*a*) are two VSF isosurfaces with different colours; the surfaces in (*b*,*c*) are colour coded by h.

For $\rho \geqslant R_v$, we have $\boldsymbol{\omega} = 0$ from (3.6). For $\rho < R_v$, substituting (3.5) and (3.6) into (3.13) yields

$$\left.\begin{aligned} \nabla \cdot (\omega_s \boldsymbol{e}_s) &= \frac{\Gamma(\rho^2 - 2\sigma^2)}{2\pi\sigma^5(1 - \kappa\rho\cos\theta)} \frac{\mathrm{d}\sigma}{\mathrm{d}s} \exp\left(\frac{-\rho^2}{2\sigma^2}\right), \\ \nabla \cdot (\omega_\rho \boldsymbol{e}_\rho) &= \frac{\Gamma(2\sigma^2 - \rho^2)}{2\pi\sigma^5(1 - \kappa\rho\cos\theta)} \frac{\mathrm{d}\sigma}{\mathrm{d}s} \exp\left(\frac{-\rho^2}{2\sigma^2}\right), \\ \nabla \cdot (\omega_\theta \boldsymbol{e}_\theta) &= 0, \end{aligned}\right\} \tag{3.14}$$

after some algebra. Finally we obtain $\nabla \cdot \boldsymbol{\omega} = 0$. ■

The numerical implementation is detailed in Appendix A. Typical examples constructed by (3.5) in figure 3 show coiled vortex lines with differential twist lying on various closed vortex tubes. Furthermore, we develop a numerical method to measure the local twisting rate on a vortex surface for given $\boldsymbol{\omega}$ and ϕ. The algorithm is based on multiple vortex lines in terms of the discrete arclength on the VSF isosurface, which is detailed in Appendix B. Thus, we can quantify the evolution of coiling vortex lines on different vortex surfaces in a viscous evolution.

4. Results

4.1. *Evolution of vortex ring with differential twist*

We highlight the role of differential twist in helicity and vortex dynamics via direct numerical simulation (DNS) of bursting of vortex rings. Initial twisted vortex rings with a radius $R_0 = 1$ are constructed by (3.5), with initial $\Gamma = \Gamma_0 = 1$ and $\sigma = \sigma_0 = 1/(8\sqrt{2\pi})$. The initial local twist rate $\eta(s, \phi_v) = \eta_0 = A\sin(s/R_0)$ varies along $\mathcal{C}$. We use the constructed vorticity fields in (3.5) as initial conditions, and calculate their evolutions using DNS. The 3-D incompressible Navier–Stokes equations are solved in the vorticity–velocity form (Wu, Ma & Zhou 2015) using the pseudo-spectral method in a periodic box of size $L = 2\pi$ on N^3 uniform grid points. The numerical solver removes aliasing errors using the two-third truncation method with the maximum wavenumber $k_{max} \approx N/3$. The time integration is treated by the explicit second-order Runge–Kutta scheme in physical space, with the adaptive time step ensuring the small enough Courant–Friedrichs–Lewy number for numerical stability and accuracy.

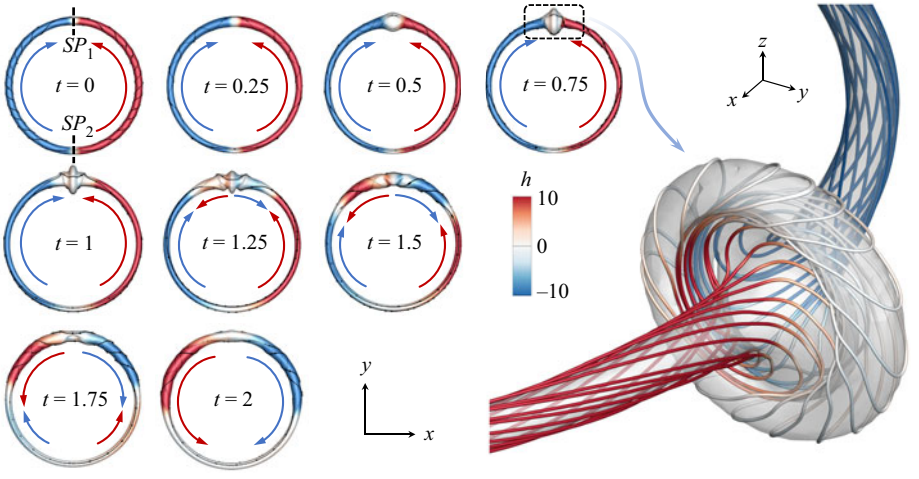

Figure 4. Lagrangian-like evolution of vortex surfaces and lines. The visualization shows the evolution of the VSF isosurface (colour coded by h) of $\phi_v = 0.5$ for $A = 20$ and $Re = 2000$. Some attached vortex lines are integrated from points on the isosurface. Note that $t = t/(R_0^2/\Gamma_0)$ is non-dimensionalized here. The close-up view shows vortex lines (colour coded by h) on the VSF isosurface (translucent) of $\phi_v = 0.7$ at $t = 0.75$ in vortex bursting.

The vortex Reynolds number is set to $Re \equiv \Gamma/\nu = 2000$. To ensure that the grid resolution can fully resolve the flow evolution, N is carefully chosen to be 512, 768 and 1024 for the initial twist amplitudes $A = 10$, 20 and 30, respectively. For each case, we carried out the grid convergence test and confirmed that the DNS results converge for N to ensure that the grid resolution fully resolves the flow evolution.

In addition, the VSF evolution is calculated using the two-time method (Yang & Pullin 2011) and its implementation is reported in Appendix C. The Lagrangian-like evolution of the twisted vortex ring with $A = 20$ and $Re = 2000$ is visualized by the isosurface of $\phi_v = 0.5$ in figure 4. At $t = 0$, two twist waves of vortex lines with opposite chiralities travel in opposite directions. Each wave packet is similar to a Kelvin wave with zero azimuthal wavenumber (Arendt *et al.* 1997; Fabre, Sipp & Jacquin 2006). Then, they collide and burst at the upper symmetric plane SP_1, forming a disk-like vortex dipole structure. Meanwhile, the axial gradient of the core size near the bursting site regenerates secondary twist waves, which propagate backward and cause secondary bursting at the lower symmetric plane SP_2 after $t = 2$. Note that, as shown in Ji & van Rees (2022) for a vortex column, such successive bursting can also be triggered by a vortex ring with initial core-size perturbation (see Appendix D).

In figure 5(a), the enstrophy $\Omega(t) = \int_{\mathcal{V}} |\boldsymbol{\omega}|^2/2 \, \mathrm{d}\mathcal{V}$ in the viscous evolution decays and shows a bump during bursting. For comparison, viscous diffusion of a vortex column shows exponential decay of Ω. Due to the initial symmetry, H remains zero, and the positive and negative parts $H^{\pm} = \int_{\mathcal{V}} h^{\pm} \, \mathrm{d}\mathcal{V}$ of H characterize the amplitudes of the counter-rotating waves. Before bursting, the core dynamics induced meridional flow (Melander & Hussain 1994) uncoils vortex lines and thickens the local vortex tube to form an axial core-size gradient. The vortex tube with the axial core-size variation then re-coils the vortex lines. Thus, $|H^{\pm}|$ first decays and then rebounds in figure 5(b). The viscous decay of $H^{\pm}$ (solid line) is faster than that of the uniform helicity model (dash-dotted line), because η, which is proportional to the viscous decay rate of twist (Yao *et al.* 2021; Shen *et al.* 2022), is more locally concentrated and larger than in the latter.

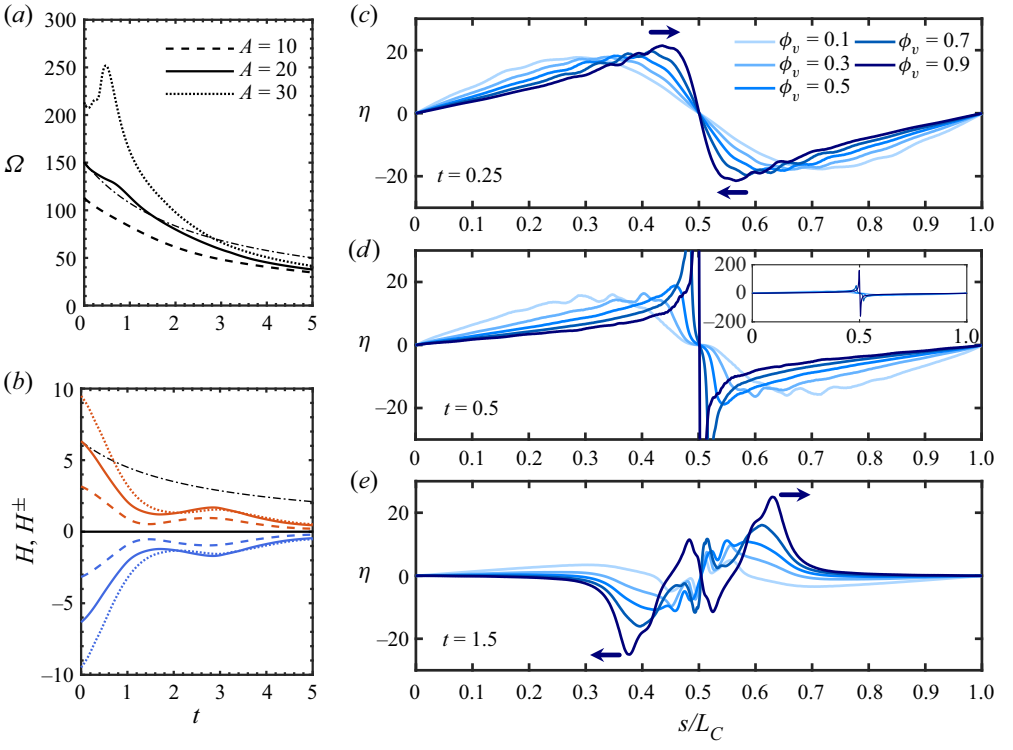

Figure 5. Flow statistics. (*a*,*b*) Evolution of (*a*) Ω and (*b*) H (black), H^+ (red) and H^- (blue) for various A. The dash-dotted lines denote modelling results $\Omega(t) = \Omega_0 \exp[-\int_0^t 2\nu(\sigma_0^2 + 2\nu t)^{-1}\,\mathrm{d}t]$ and $H(t) = H_0 \exp[-\int_0^t 2\nu(\sigma_0^2 + 2\nu t)^{-1}\,\mathrm{d}t]$ for a uniformly twisted vortex column with $A = 20$. The peak heights of Ω and $|H^{\pm}|$ grow with A, while the height of the secondary peak of $|H^{\pm}|$ is the highest for $A = 20$. (*c*–*e*) Local twist rates on different VSF isosurfaces along the vortex centreline at (*c*) $t = 0.25$, (*d*) 0.5 and (*e*) 1.5 for $A = 20$. Arrows in (*c*,*e*) denote the propagating direction of twist-wave packets. The inset in (*d*) shows entire profiles of η.

4.2. *Vortex bursting*

During the evolution, the twist propagates along $\mathcal{C}$ and varies with ϕ_v. Figure 5(*c*) plots the distribution of η along s on different vortex surfaces at $t = 0.25$ for $A = 20$ and $Re = 2000$. At early times, two peaks of η approach each other and evolve towards a discontinuity, similar to shock formation. The propagation speed of twist waves grows with ϕ_v; i.e. the waves travel faster on an inner vortex surface than on an outer surface.

We develop an inviscid model for the propagation of twist vortex waves, which can predict when the vortex bursting occurs. The twist waves are modelled as travelling waves along the vortex centreline, so that their propagation speed equals the axial velocity of the local fluid. Thus, we have

$$\eta(s, \phi_v, t) = F(s - u_s t, \phi_v), \tag{4.1}$$

with a function F. The axial velocity (Yao *et al.* 2021) of a uniformly twisted vortex tube with constant η is obtained by the Biot–Savart law as

$$u_s(\rho) = \frac{\Gamma\eta}{2\pi} \exp\left(\frac{-\rho^2}{2\sigma^2}\right). \tag{4.2}$$

Substituting the initial VSF profile $\phi_v(\rho)$ into (4.2) and replacing the constant η by a varying one yield the axial velocity

$$u_s(s, \phi_v) = \frac{\Gamma \phi_v \eta(s, \phi_v, t)}{2\pi}, \tag{4.3}$$

of a vortex surface with differential twist. Based on (4.1) and (4.3), we obtain a Burgers-like equation

$$\left.\begin{aligned} &\frac{\partial \eta}{\partial t} + \frac{\Gamma \phi_v \eta}{2\pi}\frac{\partial \eta}{\partial s} = 0, \qquad s \in [0, L_C), \quad t > 0, \\ &\eta\,(s, \phi_v, 0) = \eta_0\,(s, \phi_v)\,, \end{aligned}\right\} \tag{4.4}$$

where L_C denotes the length of $\mathcal{C}$ and $\eta_0(s, \phi_v)$ the given initial η. Note that this model is an inviscid approximation, and the twist wave can have dispersion in viscous flows.

From the solution to (4.4)

$$\eta(s, \phi_v, t) = \eta_0\left(s - \frac{\Gamma \phi_v \eta}{2\pi} t, \phi_v\right), \quad t < t_b, \tag{4.5}$$

we obtain that $\partial \eta_0/\partial s$ becomes infinite at the blow-up time

$$t_b(\phi_v) = \min\left[\left(-\frac{\Gamma \phi_v}{2\pi}\frac{\partial \eta_0}{\partial s}\right)^{-1}\right]\Bigg|_{\partial \eta_0/\partial s < 0}. \tag{4.6}$$

With $\eta_0(s, \phi_v) = A \sin(s/R_0)$, (4.6) gives an estimation of the vortex bursting time $t_b(\phi_v) = 2\pi R_0/(\Gamma_0 A \phi_v)$ for an isosurface of ϕ_v. It decreases with ϕ_v, so the bursting develops gradually from the vortex centreline to its outer surfaces, and the earliest blow-up time is $t_b(\phi_v = 1) = \pi/10 \approx 0.314$ for $A = 20$. The comparison of the DNS and modelling results for the evolution of η (see figure 6) shows that (4.5) provides a satisfactory estimate of the local twist rate.

In figure 5(*d*), the coiling of vortex lines gradually accumulates on both sides of SP_1 at $s/L_C = 0.5$ after $t = \pi/10$. The surge of η characterizes incipient vortex bursting. Consistent with the model of t_b, bursting first occurs near the vortex centreline (with large ϕ_v). In particular, the spikes of $\eta(s, \phi_v = 0.9)$ have a maximum value around 160 at $t = 0.5$ (see the inset) and are more than 10 times the averaged initial amplitude $2A/\pi$. As illustrated in the close-up view in figure 4, vortex surfaces are flattened on SP_1 and rolled up at their edge, forming a disk-like structure with highly spiral vortex lines. The local flow topology at the bursting site is similar to the statistically preferential state of the bi-axial strain in turbulence (Meneveau 2011).

The formation and decay of the disk structure significantly alter the radial tube size near SP_1, triggering the generation of secondary counter-twist waves (Ji & van Rees 2022). In figure 5(*e*), new twist waves are first generated at large ϕ_v near $\mathcal{C}$. Subsequently, the chirality of twist waves on outer vortex surfaces is reversed from inner to outer layers. The secondary twist waves gradually intensify and cause the secondary bursting on SP_2.

4.3. *Effect of initial twist amplitude*

During bursting, larger A (or higher Re) can cause a more complex vortex dynamics. Increasing A from 20 to 30 in figure 7(*a*), the VSF visualization reveals that vortex reconnection occurs within larger disk structures. As sketched in figure 7(*b*), the spiral vortex lines are pressed onto the disk, and the reconnection of each line at two locations

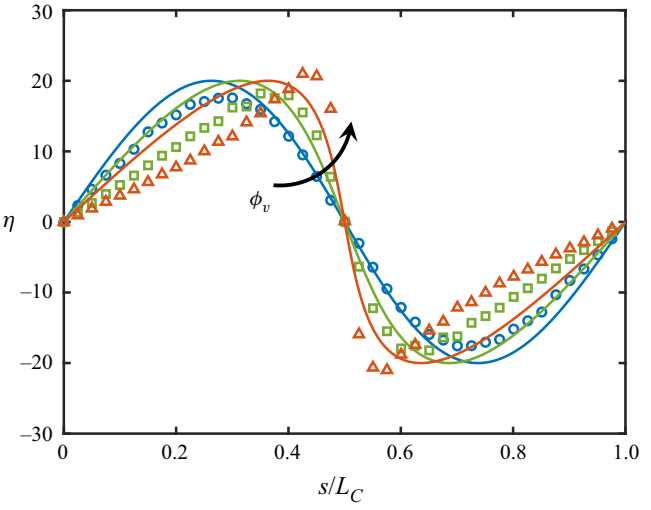

Figure 6. Comparison of DNS (symbols) and modelling (solid lines) results of η on VSF isosurfaces of $\phi_v = 0.1$ (red), 0.5 (green) and 0.9 (blue) at $t = 0.25$. The model predictions calculated from (4.5) capture different propagation speeds on different vortex surfaces, in close agreement with the DNS results.

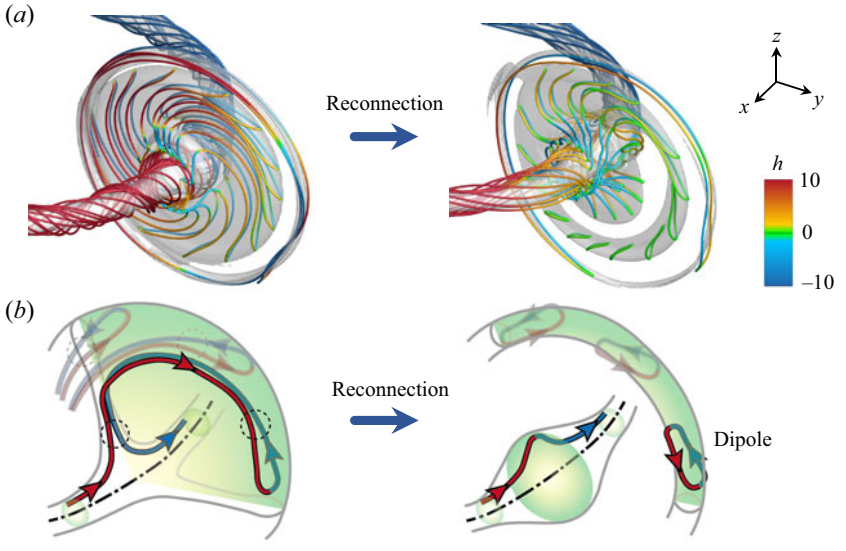

Figure 7. Vortex reconnection for the bursting vortex ring. (*a*) Evolution of the VSF isosurface $\phi_v = 0.3$ for $A = 30$ with some attached vortex lines (colour coded by h) before and after reconnection (from $t = 0.9$ to $t = 1.4$). (*b*) Schematic of the vortex reconnection that occurs in the bursting disk. Red and blue lines represent right- and left-handed coiled vortex lines, respectively. Dashed circles mark reconnection locations of a vortex line. Translucent green sections illustrate the sudden loss of the vortex tube thickness after the reconnection, where the dipole tube formed after the reconnection consists of vortex dipoles.

(marked by dashed circles) pinches off a vortex loop from the rolling-up edge of the disk. Strongly coiled vortex lines are uncoiled immediately after reconnection, causing a drop in local core size and twist rate of the main tube. The major secondary ring structure with vanishing flux consists of the pinched-off vortex loops. It is also called the vortex dipole tube (Hussain & Stout 2013) whose cross-section is a pair of concentrated vorticity

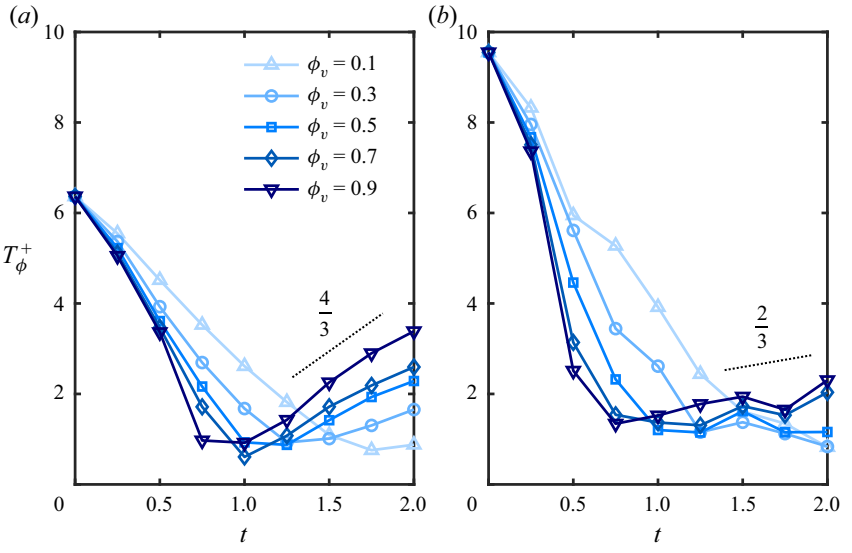

Figure 8. Effect of the vortex reconnection on the strength of twist waves. Evolution of T_ϕ^+ on different VSF isosurfaces for $A = 20$ ((*a*), without reconnection) and $A = 30$ ((*b*), with reconnection) at $Re = 2000$, along with guide lines (dotted) after the vortex bursting with slopes of $4/3$ and $2/3$, respectively.

regions with opposite signs. The successive reconnection of vortex lines is asymmetric in the θ-direction due to the curved vortex centreline, which is distinctly different from the symmetric reconnection in bursting of a rectilinear vortex tube (Ji & van Rees 2022).

In figure 5(*b*), the second peak of $|H^\pm|$ of $A = 20$ around $t = 3$ after bursting is the highest, even slightly higher than $A = 30$, implying that secondary twist waves are weakened by vortex reconnection. The amplitude of the secondary twist wave is positively correlated with the axial gradient of the vortex core size (Ji & van Rees 2022). Although stronger twist-wave collision can produce a larger disk, the reconnection significantly reduces the core size (and its axial gradient) of the disk (see figure 7*b*). After reconnection, the reduction of the core-size gradient inhibits the regeneration of strong twist waves and pre-empts subsequent bursting.

The cancellation and regeneration of right- or left-handed twist waves on different vortex surfaces can be quantified based on T_ϕ^+ or T_ϕ^-, defined as $T_\phi^\pm(\phi_v) = \oint_{\mathcal{C}} \eta^\pm \,\mathrm{d}s$ with

$$\eta^+ = \begin{cases} \eta, & \text{if } \eta \geqslant 0, \\ 0, & \text{otherwise}, \end{cases} \tag{4.7}$$

and $\eta^- = \eta - \eta^+$. The evolution of T_ϕ^+ is shown in figure 8. After the first bursting, secondary twist waves regenerate successively from inner to outer vortex surfaces. The regeneration of T_ϕ^+ for $A = 30$ with slope 2/3 is weaker than for $A = 20$ with slope 4/3, confirming weakened secondary twist waves.

5. Discussion

We develop a helicity decomposition that allows computation of the differential twist within vortex tubes. The decomposition is used to study the propagation of twist waves within a vortex ring and the bursting due to their collision. In particular, we establish a theoretical relation (2.15) between H and η of vortex lines on different coaxial vortex

surfaces, along with the numerical measurement of η based on VSF; DNS cases of bursting vortex rings are set up with differential twists. Two twist waves with opposite helical chiralities collide on the ring cross-section, where the local twist rate surges by over 10 times the average initial amplitude. The propagation speed is faster on inner vortex surfaces than on outer ones. The dynamics of vortex bursting and the bursting time are modelled by a Burgers-like equation. During the bursting, local vortex surfaces are squeezed to form a disk-like dipole structure with strongly coiled vortex lines. With larger initial twisting rates, vortex reconnection pinches dipole vortex rings off from the rolling-up edge of the bursting disk and significantly reduces the core-size gradient to inhibit subsequent bursting.

The rapid coiling and stretching of vortex lines can destabilize their vortical structures and trigger transition. As a heuristic model problem, the propagation of twist waves and bursting of a vortex ring can be further used to study extreme events of the vorticity/helicity dynamics in transition and turbulence and to explore the possible formation of finite-time singularities in the Euler dynamics. Moreover, the construction and diagnostic methods of the differential twist provide a complete framework for understanding the topological fluid dynamics of various closed vortex/magnetic tubes with delicate internal structures.

Acknowledgements. Numerical simulations were carried out on the Tianhe-2A supercomputer in Guangzhou, China.

Funding. This work has been supported by the National Natural Science Foundation of China (Grant Nos. 11925201 and 11988102), the National Key R&D Program of China (No. 2020YFE0204200) and the Xplore Prize.

Declaration of interests. The authors report no conflict of interest.

Author ORCIDs.
Weiyu Shen https://orcid.org/0000-0003-4385-8835;
Jie Yao https://orcid.org/0000-0001-6069-6570;
Fazle Hussain https://orcid.org/0000-0002-2209-9270;
Yue Yang https://orcid.org/0000-0001-9969-7431.

Author contributions. Y.Y. and W.S. designed the research. W.S. performed the research. All the authors discussed the results and wrote the manuscript. All the authors have given approval for the manuscript.

Appendix A. Numerical construction of differential twist

It is straightforward to extend the numerical algorithm in Xiong & Yang (2020) to compute the vorticity field (3.5) on a Cartesian grid. For a given closed parametric curve $\mathcal{C}: c(\zeta)$ with $\zeta \in [0, L_\zeta)$, we divide $\mathcal{C}$ into N_C segments by N_C dividing points

$$\boldsymbol{c}_i = \boldsymbol{c}(\zeta_i), \quad i = 1, 2, \ldots, N_C, \tag{A1}$$

with $\zeta_i = (i-1)\Delta\zeta$ and $\Delta\zeta = L_\zeta / N_C$. Note that ζ is not necessary to be an arclength parameter s because of the one-to-one mapping between ζ and s. Then the space in the proximity of curve $\mathcal{C}$ can be divided into N_C subdomains

$$\Omega_i = \{\boldsymbol{x} \mid (\boldsymbol{x} - \boldsymbol{c}_i) \cdot \boldsymbol{T}_i \geqslant 0 \text{ and } (\boldsymbol{x} - \boldsymbol{c}_{i+1}) \cdot \boldsymbol{T}_{i+1} < 0\}, \tag{A2}$$

with

$$\boldsymbol{T}_i = \frac{\boldsymbol{c}_{i+1} - \boldsymbol{c}_i}{|\boldsymbol{c}_{i+1} - \boldsymbol{c}_i|}, \quad i = 1, 2, \ldots, N_C, \tag{A3}$$

where subscripts $N_C + 1$ and 1 are equivalent. For a given $\boldsymbol{x}$, we first use (A2) to determine the subdomains Ω_i containing $\boldsymbol{x}$. The subscripts of all the Ω_i containing $\boldsymbol{x}$ are denoted by

a set

$$\tilde{I}_\zeta(\boldsymbol{x}) = \{j \mid \boldsymbol{x} \in \Omega_j\}. \tag{A4}$$

For each $j \in \tilde{I}_\zeta(\boldsymbol{x})$, the parameter of $\mathcal{C}$ is approximated by

$$\tilde{\zeta}_j = \frac{\zeta_{j+1}(\boldsymbol{x} - \boldsymbol{c}_j)\cdot\boldsymbol{T}_j + \zeta_j(\boldsymbol{c}_{j+1} - \boldsymbol{x})\cdot\boldsymbol{T}_j}{|\boldsymbol{c}_{j+1} - \boldsymbol{c}_j|}. \tag{A5}$$

At $\tilde{\boldsymbol{c}}_j = \boldsymbol{c}(\tilde{\zeta}_j)$, we use the second-order finite difference scheme to calculate the Frenet–Serret frame

$$\left.\begin{aligned} \tilde{\boldsymbol{T}}_j &= \boldsymbol{T}(\tilde{\zeta}_j), \\ \tilde{\boldsymbol{N}}_j &= \boldsymbol{N}(\tilde{\zeta}_j), \\ \tilde{\boldsymbol{B}}_j &= \boldsymbol{B}(\tilde{\zeta}_j), \end{aligned}\right\} \tag{A6}$$

as well as

$$\left.\begin{aligned} \tilde{\kappa}_j &= \kappa(\tilde{\zeta}_j), \\ \widetilde{\frac{\mathrm{d}\sigma}{\mathrm{d}s}}_j &= \frac{\mathrm{d}\sigma}{\mathrm{d}s}(\tilde{\zeta}_j), \end{aligned}\right\} \tag{A7}$$

in (3.5). In addition, the distance from $\boldsymbol{c}(\tilde{\zeta}_j)$ is calculated by

$$\tilde{\rho}_j = |\boldsymbol{x} - \tilde{\boldsymbol{c}}_j|, \tag{A8}$$

and azimuth-related functions are calculated by

$$\left.\begin{aligned} \cos\tilde{\theta}_j &= \frac{(\boldsymbol{x} - \tilde{\boldsymbol{c}}_j)\cdot\tilde{\boldsymbol{N}}_j}{\tilde{\rho}_j}, \\ \sin\tilde{\theta}_j &= \frac{(\boldsymbol{x} - \tilde{\boldsymbol{c}}_j)\cdot\tilde{\boldsymbol{B}}_j}{\tilde{\rho}_j}. \end{aligned}\right\} \tag{A9}$$

Finally, we approximate (3.5) as

$$\boldsymbol{\omega}(\boldsymbol{x}) = \sum_{j\in\tilde{I}_\zeta(\boldsymbol{x})} \tilde{\omega}_j, \tag{A10}$$

with

$$\tilde{\omega}_j = \left\{\begin{array}{ll} \Gamma f(\tilde{\zeta}_j, \tilde{\rho}_j)\left[\tilde{\boldsymbol{T}}_j + \dfrac{\tilde{\rho}_j}{\sigma(\tilde{\zeta}_j)(1 - \tilde{\kappa}_j\tilde{\rho}_j\cos\tilde{\theta}_j)}\widetilde{\dfrac{\mathrm{d}\sigma}{\mathrm{d}s}}_j(\cos\tilde{\theta}_j\tilde{\boldsymbol{N}}_j + \sin\tilde{\theta}_j\tilde{\boldsymbol{B}}_j)\right. & \\ \qquad \left. + \dfrac{\tilde{\rho}_j\eta(\tilde{\zeta}_j, \phi_v(\tilde{\zeta}_j, \tilde{\rho}_j))}{1 - \tilde{\kappa}_j\tilde{\rho}_j\cos\tilde{\theta}_j}(-\sin\tilde{\theta}_j\tilde{\boldsymbol{N}}_j + \cos\tilde{\theta}_j\tilde{\boldsymbol{B}}_j)\right], & 1 > \tilde{\kappa}_j\tilde{\rho}_j\cos\tilde{\theta}_j, \\ \boldsymbol{0}, & 1 \leqslant \tilde{\kappa}_j\tilde{\rho}_j\cos\tilde{\theta}_j. \end{array}\right. \tag{A11}$$

The procedure for the numerical construction of $\boldsymbol{\omega}(\boldsymbol{x})$ is summarized in Algorithm 1.

Next, we give two examples, a vortex ring and a trefoil vortex knot with varied thickness and local twist rate, to verify (2.15). The geometry of these two cases is characterized in table 1. We set $\Gamma = 1$ and $N_C = 10^6$. The maximum radius of the vortex tube is estimated

Algorithm 1: Calculation of $\boldsymbol{\omega}(\boldsymbol{x})$

Input: $\boldsymbol{x}$, $\boldsymbol{c}(\zeta)$, $\sigma(\zeta)$, $f(\zeta,\rho)$, $\phi_v(\zeta,\rho)$, $\eta(\zeta,\phi_v)$, Γ, and N_C;
Output: $\boldsymbol{\omega}(\boldsymbol{x})$;
(i) Divide the space in the proximity of curve $\boldsymbol{c}(\zeta)$ into N_C subdomains by (A2).
(ii) Obtain $\tilde{I}_\zeta$ by (A4) at $\boldsymbol{x}$.
(iii) Calculate $\tilde{\zeta}_j$ by (A5).
(iv) Calculate $\tilde{\boldsymbol{T}}_j$, $\tilde{\boldsymbol{N}}_j$ and $\tilde{\boldsymbol{B}}_j$ by (A6).
(v) Calculate $\tilde{\kappa}_j$ and $\dfrac{\widetilde{\mathrm{d}\sigma}}{\mathrm{d}s_j}$ by (A7);
(vi) Calculate $\tilde{\rho}_j$ by (A8).
(vii) Calculate $\cos\tilde{\theta}_j$ and $\sin\tilde{\theta}_j$ by (A9).
(viii) Calculate $\boldsymbol{\omega}(\boldsymbol{x})$ by (A10) with computed and given variables.

Case	$\boldsymbol{c}(\zeta)$	$\sigma(\zeta)$	$\eta(\zeta,\phi_v)$
1	$c_x(\zeta)=\cos(\zeta)$ $c_y(\zeta)=\sin(\zeta)$ $c_z(\zeta)=0$	$\dfrac{2+\sin(5\zeta)}{8\sqrt{2\pi}}$	$20\phi_v\sin(\zeta/2)$
2	$c_x(\zeta)=(1+0.5\cos(3\zeta))\cos(2\zeta)$ $c_y(\zeta)=(1+0.5\cos(3\zeta))\sin(2\zeta)$ $c_z(\zeta)=-0.5\sin(3\zeta)$	$\dfrac{3+\sin(6\zeta)}{16\sqrt{2\pi}}$	$10\sin(\pi\phi_v)(1+2\sin(3\zeta))$

Table 1. Geometric parameters.

as $R_v = 5\max[\sigma(s)]$. Over 99.999 % of the vorticity magnitude in (3.5) is contained in the tube with R_v, so we consider this vorticity field as compactly supported.

We construct the vortex tubes in a periodic box of side $L = 2\pi$ and use 512^3 grid points. The velocity field is calculated from the vorticity via the Biot–Savart law in Fourier space (Xiong & Yang 2019). Note that the cutoff of the Gaussian tail at R_v in (3.6) has a negligible influence on the smoothness of the initial vorticity. The total helicity H is obtained by numerically integrating the helicity density over the periodic box on the 3-D Cartesian grid. The writhing number is calculated by

$$W_r = \frac{1}{4\pi}\oint_{\mathcal{C}}\oint_{\mathcal{C}}\frac{(\boldsymbol{x}-\boldsymbol{x}^*)\cdot\mathrm{d}\boldsymbol{x}\times\mathrm{d}\boldsymbol{x}^*}{|\boldsymbol{x}-\boldsymbol{x}^*|^3} = \frac{1}{4\pi}\oint_{\mathcal{C}}\oint_{\mathcal{C}}\frac{[\boldsymbol{c}(\zeta)-\boldsymbol{c}(\xi)]\cdot[\boldsymbol{c}'(\zeta)\times\boldsymbol{c}'(\xi)]}{|\boldsymbol{c}(\zeta)-\boldsymbol{c}(\xi)|^3}\,\mathrm{d}\zeta\,\mathrm{d}\xi, \tag{A12}$$

where $\boldsymbol{x}$ and $\boldsymbol{x}^*$ denote two points on $\mathcal{C}$. The two cases are visualized in figure 9 using VSF isosurfaces colour coded by h with attached vortex lines. Their total helicity and writhe number numerical calculated by (2.1) and (A12) are listed in table 2.

For the two closed vortex tubes, we verify (2.14) by comparing results of (2.14) and $H/\Gamma^2 - W_r$ listed in table 2. The former is directly calculated by (2.14), and the latter is calculated by the Călugăreanu–White theorem (Moffatt & Ricca 1992) using the vorticity fields on the numerical Cartesian grid. For the vortex tube constructed by (3.5), the

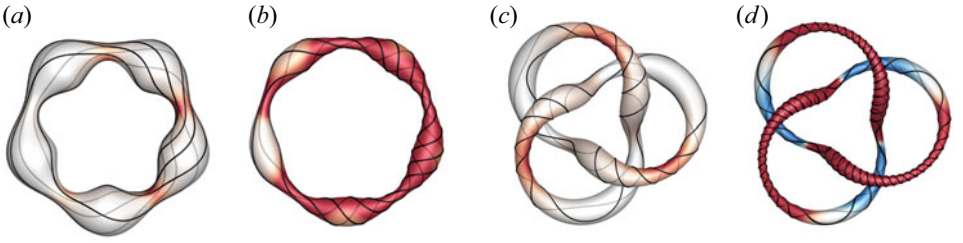

Figure 9. The VSF isosurfaces (colour coded by h) of (a,c) $\phi_v = 0.1$ and (b,d) 0.5 with some attached vortex lines for the ring and trefoil knot listed in table 1.

Case	H	W_r	$T_w = H/\Gamma^2 - W_r$	T_w calculated by (A16)
1	4.244	0	4.244	4.244
2	19.678	3.518	16.160	16.160

Table 2. Total helicity and writhe number calculated by (2.1) and (A12).

circulation for the isosurface of ϕ_v in (3.7) is

$$\Gamma_\phi(\phi_v) = \int_{S_\phi} \boldsymbol{\omega}\cdot\boldsymbol{e}_s \,\mathrm{d}S = \int_{S_\phi} \omega_s \,\mathrm{d}S, \tag{A13}$$

where S_ϕ denotes the area enclosed by the isosurface of ϕ_v on S_C. The cross-section of the tube on S_C is circular with radius

$$\rho_\phi(s,\phi_v) = \sqrt{-2\sigma(s)^2\ln\phi_v}. \tag{A14}$$

Substituting (3.5) and (A14) into (A13) yields

$$\Gamma_\phi(\phi_v) = \int_{S_\phi} \frac{\Gamma}{2\pi\sigma(s)^2}\exp\left[\frac{-\rho^2}{2\sigma(s)^2}\right]\mathrm{d}S = \Gamma(1-\phi_v). \tag{A15}$$

Substituting (A15) and $\mathrm{d}s = |\mathrm{d}\boldsymbol{c}(\zeta)/\mathrm{d}\zeta|\,\mathrm{d}\zeta$ into (2.15) yields

$$T_w = \frac{1}{\pi}\int_0^1 (1-\phi_v)\left(\oint_C \eta(\zeta,\phi_v)\left|\frac{\mathrm{d}\boldsymbol{c}(\zeta)}{\mathrm{d}\zeta}\right|\mathrm{d}\zeta\right)\mathrm{d}\phi_v. \tag{A16}$$

Using (A16), we obtain

$$T_w = \frac{40}{3\pi} \approx 4.244, \tag{A17}$$

for case 1 in table 1, and

$$T_w = \frac{10}{\pi^2}\int_0^{2\pi}\sqrt{\cos^2(3\zeta)+4\cos(3\zeta)+\frac{25}{4}}\,\mathrm{d}\zeta \approx 16.160, \tag{A18}$$

for case 2. The excellent agreement of these theoretical results and the numerical ones in table 2 demonstrates that the description of the differential twist in (2.14) is complete and accurate.

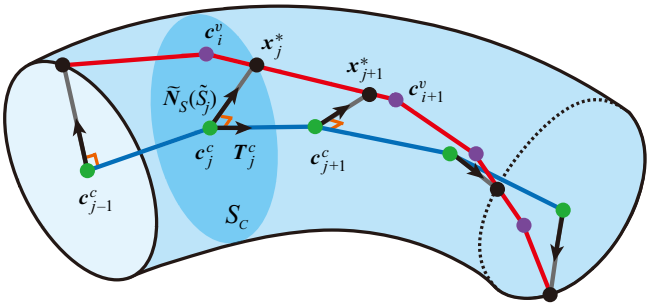

Figure 10. Schematic for determining $\tilde{N}_s(\tilde{s}_j)$ from the discrete vortex centreline (blue) pointing to a discrete vortex line (red).

Appendix B. Numerical measurement of the local twist rate

We develop a numerical method to measure the local twisting rate on a vortex surface for given $\boldsymbol{\omega}$ and ϕ. As illustrated in figure 10, the algorithm for measuring $\eta(\tilde{s}_j, \Phi)$ is based on the discrete arclength parameter $\tilde{s}_j$ on the isosurface of $\phi_v = \Phi$.

For a given $\phi_v = \Phi$, we integrate a vortex line $\mathcal{C}_v$ on the isosurface of $\phi_v(\boldsymbol{x}) = \Phi$ with a sequence of discrete points $\boldsymbol{c}_i^v, i = 1, 2, \ldots, N_v$. Then $\mathcal{C}_v$ can be divided into N_v line segments

$$L_i = \{\boldsymbol{x} \mid \boldsymbol{x} = \boldsymbol{c}_i^v + p(\boldsymbol{c}_{i+1}^v - \boldsymbol{c}_i^v), \quad p \in [0, 1)\}, \quad i = 1, 2, \ldots, N_v, \tag{B1}$$

where subscripts $N_v + 1$ and 1 are equivalent. For the present VSF, $\phi_v = 1$ represents the vortex centreline. We integrate a limiting vortex line on the isosurface of $\phi_v(\boldsymbol{x}) \to 1$, as an approximation of $\mathcal{C}$, with a sequence of discrete points $\boldsymbol{c}_j^c, j = 1, 2, \ldots, N_c$. Note that this centreline identification method is essentially the same as that in Kerr (2018*a*) for the vortex tubes with the VSF and axial vorticity maxima on the vortex centreline.

Each $\boldsymbol{c}_j^c$ corresponds to a vortex line segment $L_j^* = L_i$ where the intersection of S_C and $\mathcal{C}_v$ is located, and this segment can be determined by searching

$$(\boldsymbol{c}_i^v - \boldsymbol{c}_j^c) \cdot \boldsymbol{T}_j^c \leqslant 0 \text{ and } (\boldsymbol{c}_{i+1}^v - \boldsymbol{c}_j^c) \cdot \boldsymbol{T}_j^c \geqslant 0, \tag{B2}$$

with

$$\boldsymbol{T}_j^c = \frac{\boldsymbol{c}_{j+1}^c - \boldsymbol{c}_j^c}{|\boldsymbol{c}_{j+1}^c - \boldsymbol{c}_j^c|}, \quad j = 1, 2, \ldots, N_c, \tag{B3}$$

where subscripts $N_c + 1$ and 1 are equivalent. Thus the intersection $\boldsymbol{x}_j^*$ of S_C and $\mathcal{C}_v$ is calculated by

$$(\boldsymbol{x}_j^* - \boldsymbol{c}_j^c) \cdot \boldsymbol{T}_j^c = 0, \quad \boldsymbol{x}_j^* \in L_j^*. \tag{B4}$$

Then, we obtain the unit vector $\tilde{\boldsymbol{N}}_s(\tilde{s}_j)$ at $\boldsymbol{c}_j^c$ pointing to $\boldsymbol{x}_j^*$ on the isosurface of $\phi_v = \Phi$ by

$$\tilde{\boldsymbol{N}}_s(\tilde{s}_j) = \frac{\boldsymbol{x}_j^* - \boldsymbol{c}_j^c}{|\boldsymbol{x}_j^* - \boldsymbol{c}_j^c|}, \quad j = 1, 2, \ldots, N_c, \tag{B5}$$

and

$$\left.\begin{aligned} \tilde{\boldsymbol{N}}_s(\tilde{s}_{N_c+1}) &= \tilde{\boldsymbol{N}}_s(\tilde{s}_i), \\ \tilde{\boldsymbol{N}}_s(\tilde{s}_0) &= \tilde{\boldsymbol{N}}_s(\tilde{s}_{N_c}), \end{aligned}\right\} \tag{B6}$$

with a discrete arclength parameter

$$\tilde{s}_j = \begin{cases} -|\boldsymbol{c}^c_{N_c} - \boldsymbol{c}^c_1|, & j = 0, \\ 0, & j = 1, \\ \displaystyle\sum_{k=2}^{j} |\boldsymbol{c}^c_k - \boldsymbol{c}^c_{k-1}|, & j = 2, 3, \ldots, N_c, \\ |\boldsymbol{c}^c_{N_c} - \boldsymbol{c}^c_1| + \displaystyle\sum_{k=2}^{j} |\boldsymbol{c}^c_k - \boldsymbol{c}^c_{k-1}|, & j = N_c + 1. \end{cases} \tag{B7}$$

Finally, the local twist rate on the isosurface of $\phi_v = \Phi$ is approximated by

$$\eta\left(\tilde{s}_j, \Phi\right) = \left(\tilde{\boldsymbol{N}}_s(\tilde{s}_j) \times \frac{\tilde{\boldsymbol{N}}_s(\tilde{s}_{j+1}) - \tilde{\boldsymbol{N}}_s(\tilde{s}_{j-1})}{s_{j+1} - s_{j-1}}\right) \cdot \boldsymbol{T}^c_j. \tag{B8}$$

The procedure for the numerical measurement of $\eta(\tilde{s}_j, \Phi)$ is summarized in Algorithm 2. An ideal measurement of η needs to sample all the vortex lines uniformly covering the entire vortex surface. In the practical measurement, we select a finite number of vortex lines, e.g. eight in the present study, on a vortex surface. The seeding points for integrating vortex lines are uniformly distributed on the cross-section SP_2.

Algorithm 2: Calculation of $\eta(\tilde{s}_j, \Phi)$

Input: $\boldsymbol{c}^c$, $\boldsymbol{c}^v$;
Output: $\eta(\tilde{s}_j, \Phi)$;
(i) **for** $j \leftarrow 1$ **to** N_c
(ii) Calculate $\boldsymbol{T}^c_j$ by (B3);
(iii) **for** $i \leftarrow 1$ **to** N_v
(iv) **if** (B2) **then**
(v) Calculate $\boldsymbol{x}^*_j$ by (B4);
(vi) **break**
(vii) **end**
(viii) **end**
(ix) Calculate $\tilde{s}_j$ by (B7);
(x) Calculate $\tilde{\boldsymbol{N}}_s$ by (B5) and (B6);
(xi) **end**
(xii) Calculate $\eta(\tilde{s}_j, \Phi)$ by (B8) with computed variables.

Appendix C. The VSF calculation

The VSF is defined to satisfy the constraint $\boldsymbol{\omega} \cdot \nabla\phi_v = 0$. The two-time method (Yang & Pullin 2011) is used to calculate the Lagrangian-like evolution of VSFs, which involves prediction and correction substeps for each physical time step. The local deviation (Yang & Pullin 2010) of the numerical VSF solution ϕ_v from an exact VSF is defined as $\lambda_\omega = \boldsymbol{\omega} \cdot \nabla\phi_v / (|\boldsymbol{\omega}|\,|\nabla\phi_v|)$. The volume-averaged VSF deviation $\langle|\lambda_\omega|\rangle$ for all cases are less than 0.3 % in the entire evolution, which is very accurate for identifying vortex surfaces.

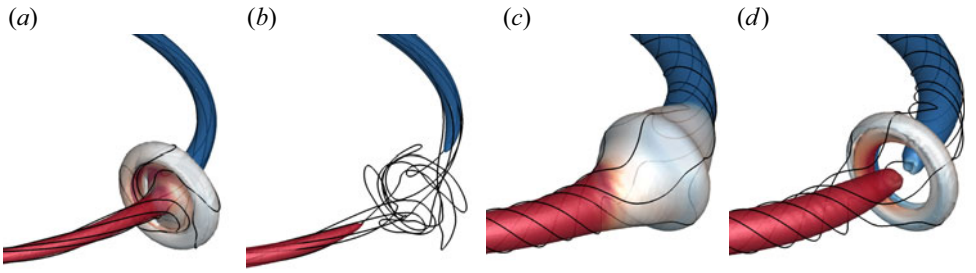

Figure 11. Comparison of isosurfaces of the VSF and the vorticity magnitude at $t = 0.75$ for $A = 20$ and $Re = 2000$: (*a*) $\phi_v = 0.75$, (*b*) $|\boldsymbol{\omega}| = 50$, (*c*) $\phi_v = 0.25$ and (*d*) $|\boldsymbol{\omega}| = 20$. Some vortex lines are integrated from points on the surfaces colour coded by h.

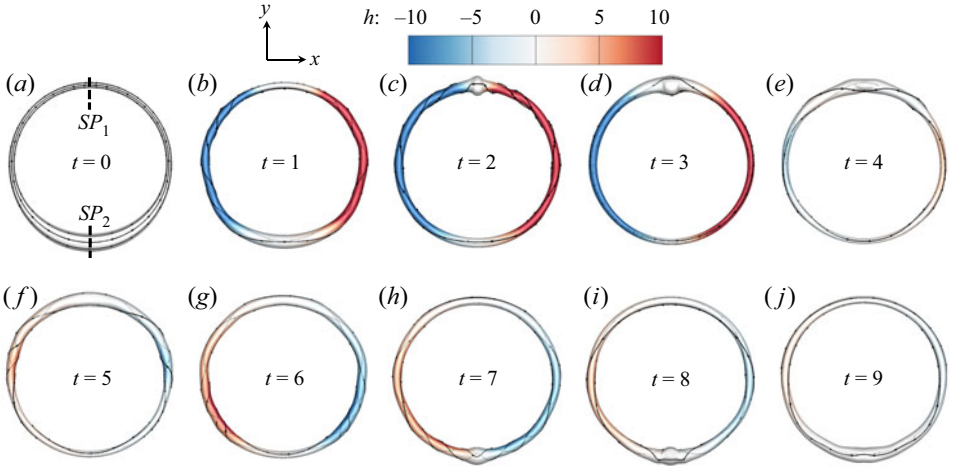

Figure 12. Evolution of the VSF isosurface (colour coded by h) of $\phi_v = 0.75$ with some attached vortex lines for the bursting vortex ring with the initial core-size perturbation at $Re = 2000$.

Note that the visualization of Eulerian vortex criteria, e.g. the visual breakup of isosurfaces of $|\boldsymbol{\omega}|$ in figure 11(*b*,*c*), cannot identify the complete vortex tube as visualized by the VSF in figure 11(*a*,*b*) during bursting.

Appendix D. Bursting vortex ring with initial core-size perturbation

We illustrate the bursting vortex ring due to the initial core-size perturbation. This type of vortex bursting was observed in vortex columns (van Rees 2020; Stout 2021; Ji & van Rees 2022). Based on (3.5), we set a varying initial core size

$$\sigma(s) = \begin{cases} \dfrac{1}{8\sqrt{2\pi}}, & s \in [0, \pi), \\ \dfrac{2 - \cos(2s)}{8\sqrt{2\pi}}, & s \in [\pi, 2\pi), \end{cases} \tag{D1}$$

and $\eta_0 = 0$ and $\Gamma = 1$. The initial configuration is shown by the VSF isosurface in figure 12(*a*). Note that the ratio of the maximum to minimum core size is three, consistent with Ji & van Rees (2022).

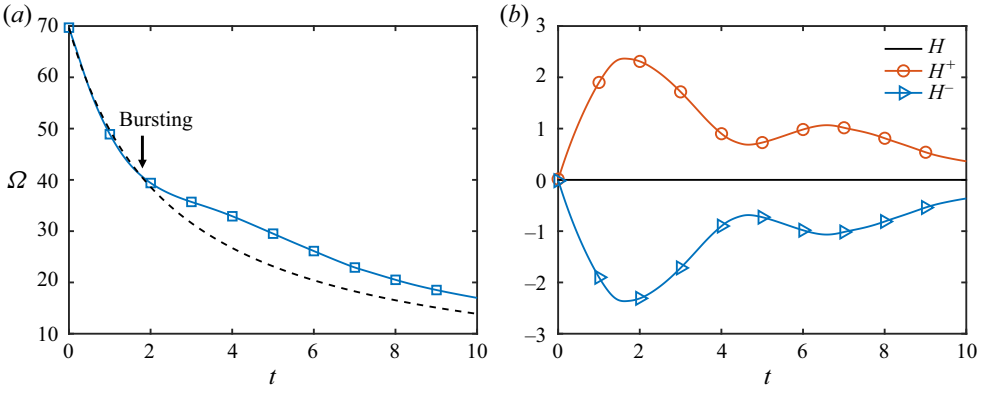

Figure 13. Evolution of the enstrophy and helicity for the core-size perturbation case at $Re = 2000$. The dashed line in (a) denotes the modelling result $\Omega(t) = \Omega_0 \exp[-\int_0^t 2\nu(\sigma_0^2 + 2\nu t)^{-1}\,\mathrm{d}t]$ for a uniformly twisted vortex column.

The evolution of the VSF isosurface at $Re = 2000$ is depicted in figure 12. Due to the axial gradient of the initial core size, two counter-rotating twist waves are generated and then collide on the symmetric plane SP_1 to cause vortex bursting. As the disk-shaped structure is generated and then dissipated, secondary twist waves are generated to trigger the secondary bursting at SP_2. In the later evolution, successive burstings occur on alternate planes SP_1 and SP_2. The enhancement of the local vorticity magnitude in the vortex bursting causes the bump in the profile of Ω in figure 13(a), which is similar to that in figure 4(a). Different from the case of initial twist waves in figure 4(b), H^+ and H^- first grow with the self-generation and enhancement of twist waves, and then decay and oscillate with multiple burstings and regenerations of twist waves in figure 13(b).

Note that the direct construction of twist waves is more suitable than setting the initial core-size perturbation in terms of precisely controlling the amplitude and distribution of twist waves for quantitative studies.

References

Angriman, S., Cobelli, P.J., Bourgoin, M., Huisman, S.G., Volk, R. & Mininni, P.D. 2021 Broken mirror symmetry of tracer's trajectories in turbulence. *Phys. Rev. Lett.* **127** (25), 254502.

Arendt, S., Fritts, D.C. & Andreassen, Ø. 1997 The initial value problem for Kelvin vortex waves. *J. Fluid Mech.* **344**, 181–212.

Buaria, D. & Pumir, A. 2022 Vorticity-strain rate dynamics and the smallest scales of turbulence. *Phys. Rev. Lett.* **128** (9), 094501.

Chui, A.Y.K. & Moffatt, H.K. 1995 The energy and helicity of knotted magnetic flux tubes. *Proc. R. Soc. Lond.* A **451**, 609–629.

Cirtain, J.W., *et al.* 2013 Energy release in the solar corona from spatially resolved magnetic braids. *Nature* **493**, 501–503.

Cuypers, Y., Maurel, A. & Petitjeans, P. 2003 Vortex burst as a source of turbulence. *Phys. Rev. Lett.* **91** (19), 194502.

Fabre, D., Sipp, D. & Jacquin, L. 2006 Kelvin waves and the singular modes of the Lamb–Oseen vortex. *J. Fluid Mech.* **551**, 235–274.

Fritts, D.C., Arendt, S. & Andreassen, Ø. 1998 Vorticity dynamics in a breaking internal gravity wave. Part 2. Vortex interactions and transition to turbulence. *J. Fluid Mech.* **367**, 47–65.

Fuller, F.B. 1971 The writhing number of a space curve. *Proc. Natl Acad. Sci. USA* **68**, 815–819.

Hussain, A.K.M.F. 1986 Coherent structures and turbulence. *J. Fluid Mech.* **173**, 303–356.

Hussain, F. & Stout, E. 2013 Self-limiting and regenerative dynamics of perturbation growth on a vortex column. *J. Fluid Mech.* **718**, 39–88.

JI, L. & VAN REES, W.M. 2022 Bursting on a vortex tube with initial axial core-size perturbations. *Phys. Rev. Fluids* **7**, 044704.
KERR, R.M. 2018*a* Topology of interacting coiled vortex rings. *J. Fluid Mech.* **854**, R2.
KERR, R.M. 2018*b* Enstrophy and circulation scaling for Navier–Stokes reconnection. *J. Fluid Mech.* **839**, R2.
KLECKNER, D. & IRVINE, W.T.M. 2013 Creation and dynamics of knotted vortices. *Nat. Phys.* **9** (4), 253–258.
KLECKNER, D., KAUFFMAN, L.H. & IRVINE, W.T.M. 2016 How superfluid vortex knots untie. *Nat. Phys.* **12**, 650–655.
KOPLIK, J. & LEVINE, H. 1996 Scattering of superfluid vortex rings. *Phys. Rev. Lett.* **76** (25), 4745.
LEIBOVICH, S. 1978 The structure of vortex breakdown. *Annu. Rev. Fluid Mech.* **10** (1), 221–246.
MAYER, E.W. & POWELL, K.G. 1992 Viscous and inviscid instabilities of a trailing vortex. *J. Fluid Mech.* **245**, 91–114.
MELANDER, M.V. & HUSSAIN, F. 1994 Core dynamics on a vortex column. *Fluid Dyn. Res.* **13** (1), 1–37.
MENEVEAU, C. 2011 Lagrangian dynamics and models of the velocity gradient tensor in turbulent flows. *Annu. Rev. Fluid Mech.* **43**, 219–245.
MENG, Z., SHEN, W. & YANG, Y. 2023 Evolution of dissipative fluid flows with imposed helicity conservation. *J. Fluid Mech.* **954**, A36.
MOFFATT, H.K. 1969 The degree of knottedness of tangled vortex lines. *J. Fluid Mech.* **35**, 117–129.
MOFFATT, H.K. 2021 Extreme events in turbulent flow. *J. Fluid Mech.* **914**, F1.
MOFFATT, H.K., KIDA, S. & OHKITANI, K. 1994 Stretched vortices – the sinews of turbulence; large-Reynolds-number asymptotics. *J. Fluid Mech.* **259**, 241–264.
MOFFATT, H.K. & RICCA, R.L. 1992 Helicity and the Călugăreanu invariant. *Proc. R. Soc. Lond.* A **439**, 411–429.
MOFFATT, H.K. & TSINOBER, A. 1992 Helicity in laminar and turbulent flow. *Annu. Rev. Fluid Mech.* **24**, 281–312.
MOREAU, J.J. 1961 Constantes d'un îlot tourbillonnaire en fluide parfait barotrope. *C. R. Hebd. Seances Acad. Sci.* **252**, 2810–2812.
PRADEEP, D.S. & HUSSAIN, F. 2001 Core dynamics of a strained vortex: instability and transition. *J. Fluid Mech.* **447**, 247–285.
PULLIN, D.I. & SAFFMAN, P.G. 1998 Vortex dynamics in turbulence. *Annu. Rev. Fluid Mech.* **30**, 31–51.
VAN REES, W.M. 2020 Vortex bursting. *Phys. Rev. Fluids* **5** (11), 110504.
RICCA, R.L., SAMUELS, D.C. & BARENGHI, C.F. 1999 Evolution of vortex knots. *J. Fluid Mech.* **391**, 29–44.
ROBINSON, S.K. 1991 Coherent motions in the turbulent boundary layer. *Annu. Rev. Fluid Mech.* **23** (1), 601–639.
RUAN, S., XIONG, S., YOU, J. & YANG, Y. 2022 Generation of streamwise helical vortex loops via successive reconnections in early pipe transition. *Phys. Fluids* **34** (5), 054112.
SCHEELER, M.W., VAN REES, W.M., KEDIA, H., KLECKNER, D. & IRVINE, W.T.M. 2017 Complete measurement of helicity and its dynamics in vortex tubes. *Science* **357**, 487–491.
SHARIFF, K. & LEONARD, A. 1992 Vortex rings. *Annu. Rev. Fluid Mech.* **24** (1), 235–279.
SHEN, W., YAO, J., HUSSAIN, F. & YANG, Y. 2022 Topological transition and helicity conversion of vortex knots and links. *J. Fluid Mech.* **943**, A41.
STOUT, E. 2021 Genesis and evolution of vortex bursting. PhD thesis, Texas Tech University.
TOMBACH, I. 1973 Observations of atmospheric effects on vortex wake behavior. *J. Aircraft* **10** (11), 641–647.
WU, J.-Z., MA, H.-Y. & ZHOU, M.-D. 2015 *Vortical Flows*, vol. 28. Springer.
XIONG, S. & YANG, Y. 2019 Construction of knotted vortex tubes with the writhe-dependent helicity. *Phys. Fluids* **31**, 047101.
XIONG, S. & YANG, Y. 2020 Effects of twist on the evolution of knotted magnetic flux tubes. *J. Fluid Mech.* **895**, A28.
YANG, Y. & PULLIN, D.I. 2010 On Lagrangian and vortex-surface fields for flows with Taylor–Green and Kida–Pelz initial conditions. *J. Fluid Mech.* **661**, 446–481.
YANG, Y. & PULLIN, D.I. 2011 Evolution of vortex-surface fields in viscous Taylor–Green and Kida–Pelz flows. *J. Fluid Mech.* **685**, 146–164.
YAO, J. & HUSSAIN, F. 2022 Vortex reconnection and turbulence cascade. *Annu. Rev. Fluid Mech.* **54**, 317–347.
YAO, J., SHEN, W., YANG, Y. & HUSSAIN, F. 2022 Helicity dynamics of viscous vortex links. *J. Fluid Mech.* **944**, A41.
YAO, J., YANG, Y. & HUSSAIN, F. 2021 Dynamics of a trefoil knotted vortex. *J. Fluid Mech.* **923**, A19.

ZHAO, X., YU, Z., CHAPELIER, J.-B. & SCALO, C. 2021 Direct numerical and large-eddy simulation of trefoil knotted vortices. *J. Fluid Mech.* **910**, A31.

ZHENG, W., YANG, Y. & CHEN, S. 2016 Evolutionary geometry of Lagrangian structures in a transitional boundary layer. *Phys. Fluids* **28**, 035110.